



## Independent Component Analysis of Hyperion Data to Map Alteration Zones

MAJID M. OSKOEI, Tabriz, Iran

**Keywords:** Remote Sensing, ICA, Hyperspectral, Hyperion, Mineral detection, Mapping

**Summary:** We present an improved method for independent component analysis aiming to detect minerals in the Erongo complex, Namibia. We evaluate independent component analysis (ICA) to detect and map alteration halos in Erongo Namibia using the Hyperion dataset. Detailed surveys and investigations are possible given the capability of the hyperspectral sensors to render a great deal of spectral information by observing the surface of earth. In terms of mineral detection, however, there are particular challenges. In this research, we used two methods to achieve an independent components (ICs) map. The first method computes the virtual dimensionality (VD) of a dataset, prioritises calculated ICs, and finally picks up only a certain number of ICs. This number is equal to the calculated VD. Since some ICs share extreme pixels, the final extremes from this method are less than the VD. The presented modified method differs slightly from the first one. In this method, extreme pixels for all ICs are determined, and all ICs with the same extreme pixels are considered equal. Prioritisation of IC bands takes place afterward. The results demonstrate that the second method performs better because in addition to its ability to map more end-members, the mapped zones match lithological structures better. The dataset is atmospherically corrected by ACORN, and data quality assessment is performed to discriminate bad bands before ICA. To determine each extreme pixel mineralogical, spectral feature fitting (SFF) algorithm was used in the SWIR range of electromagnetic wavelength by comparing to USGS mineral spectral library.

**Zusammenfassung:** Analyse unabhängiger Komponenten von Hyperion Daten zur Kartierung von Verwitterungszonen in Erongo, Namibia. Wir präsentieren ein verbessertes Verfahren für die Analyse unabhängiger Komponenten (ICA) mit dem Ziel der Mineral-Erkennung im Erongo Komplex. Detail-Untersuchungen sind unter Verwendung von Hyperspektral-Sensoren möglich, weil diese Sensoren eine große Leistungsfähigkeit in der Wiedergabe der Spektralinformation der Erdoberfläche besitzen. Bei der Mineral-Erkennung gibt es jedoch besondere Herausforderungen. In dieser Untersuchung wurden zwei Methoden zur Erzeugung einer unabhängigen Komponenten (IC) Karte berücksichtigt. Die erste Methode berechnet die virtuelle Dimensionalität (VD) des Datensatzes, priorisiert berechnete ICs, und verwendet schließlich nur eine bestimmte Anzahl von ICs. Diese Anzahl entspricht der berechneten VD. Da sich einige ICs extreme Pixel teilen, sind die endgültigen Extrema bei dieser Methode weniger als bei der VD. Die vorgestellte Methode unterscheidet sich ein wenig von der ersten. Bei ihr werden extreme Pixel für alle ICs bestimmt, und alle ICs mit den gleichen extremen Pixeln werden als gleich angesehen. Die Priorisierung von ICs Bands erfolgt später. Die Ergebnisse zeigen, dass die zweite Methode eine höhere Leistungsfähigkeit besitzt, weil zusätzlich zu der Fähigkeit, mehr Endmember zu kartieren, die zugeordneten Zonen besser zu den lithologischen Strukturen passen. Der Datensatz wird atmosphärisch mit ACORN verbessert und es wurde eine Bewertung der Datenqualität durchgeführt, um schlechte Bänder vor der ICA zu unterscheiden. Für die Detektion von Mineralien wird in jedem extremen Pixel ein spektraler Merkmalsanpassung (SFF) Algorithmus im SWIR Band verwendet, indem mit der USGS Mineral-Bibliothek verglichen wird.

## 1 Introduction

Independent Component Analysis (ICA) has been widely used in various blind source separations. Its application to linear spectral mixture analysis in remote sensing and image processing has shown promising results (BAYLISS et al. 1997, CHIANG et al. 2000, LENNON et al. 2001, BOTCHKO et al. 2003, WANG & CHANG 2006a, DU et al. 2006). Independent Component Analysis addresses the problem of determining the factors that contribute independently (in a statistical sense) to observed data from a set of sensors. So far, considering the linear mixture model, in contrast to other approaches, ICA assumes that the abundance fractions that are commonly assumed to be unknown and non-random constants are now random parameters and statistically independent signal sources. In addition, one signal source at the most is allowed to be Gaussian (VARSHNEY & ARORA 2004). These two assumptions should be closely considered in the unmixing procedure when violating of them could result in estimation errors.

ICA is known as a blind source separation, so it is possible to achieve estimation for end-members themselves. If we assume that observations or  $R$ s are noise-free ( $R=aE$ ), then there is a matrix  $W$

$$\text{where } E = WR \quad (1)$$

With regard to the ICA concept (independent components), the matrix  $W$  can be determined by solving an optimisation problem that aims to minimise mutual information between components (VARSHNEY & ARORA 2004, HYVÄRINEN 1999).

It is important in practice to make learning faster and more reliable. This can be achieved using fixed-point iteration algorithms. In these algorithms, the computations are made in batch (or block) mode, i. e., a large number of data points are used in a single step of the algorithm. In other respects, however, these algorithms may be considered neural. In particular, they are parallel, distributed, computationally simple, and require little memory space. HYVÄRINEN (1999) showed that fixed-point algorithms have very appealing convergence properties, making them an interesting alternative to adaptive learning rules

in environments where fast real-time adaptation is not necessary. Note that their basic ICA algorithms require a preliminary sphering or whitening of the data  $R$ . Sphering means that the original observed variable, e. g.,  $v$ , is linearly transformed to a variable  $R = Qv$  such that the correlation matrix of  $R$  equals unity:  $E\{RR^T\} = I$ .

### 1.1 Study Area

The study area is located in north-western Namibia and includes the Erongo Complex with a diameter of approximately 35 km; this is one of the largest Cretaceous anorogenic complexes in that country. The centre of the complex is located at approximately 21°40' S and 15°38' E (cf. Fig. 1).

This represents the eroded core of a caldera structure with peripheral and central granitic intrusions. Surrounding the outer granitic intrusions of the Erongo Complex is a ring dike of olivine dolerite that locally reaches some 200 m in thickness and has a radius of 32 km. The ring dike weathers easily and is therefore highly eroded. However, it can be easily identified in aeromagnetic data and satellite images.

The central part of the Erongo complex consists of a layered sequence of volcanic rocks that form prominent cliffs rising several hundred meters above the surrounding basement. The basement rocks consist of mica schists and meta-greywackes of the Kuiseb Formation and various intrusions of granites. In the southeast, the rocks of the Erongo Complex overlie the Triassic Lions Head Formation, which consists of conglomerates, gritstone, arkose with interbedded siltstone and mudstone, and quartz arenite (SCHNEIDER & SCHNEIDER 2004).

### 1.2 Pre-processing

There are some essential processes that must be done on the data before main processing concerning on the sensor type and its technical specifications. The pre-processing includes algorithms to correct probable errors that occur during image acquisition. Vertical destriping, georeferencing, atmospheric correction,

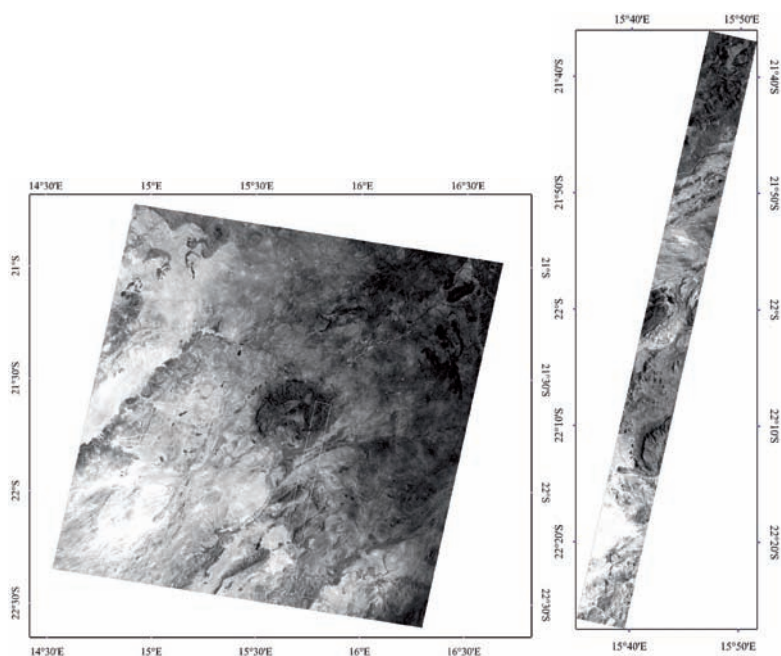


**Fig. 1:** ETM scene of the Erongo complex and location of the Hyperion scene (left) in addition to Hyperion band 28 (right).

and spectral profile enhancement (or polishing) are the corrections that were performed on the Hyperion data.

Vertical stripes usually occur in several columns with constant Digital Number (DN) because of technical failure in the functionality of some detectors and they were removed by averaging the neighbouring columns.

Georeferencing of the data is performed just before producing final map to prevent possible errors that resampling and approximating make in the data and will therefore affect functionality of other processing tasks. The Hyperion data was registered with the use of the ETM image of Erongo that had been supplied georeferenced.

The smile effect (line curvature) on the Hyperion data is an across track shift from a centre wavelength because of changes in dispersion angle. This is negligible in the SWIR range of the spectra (less than 1 nm), but variables in the VNIR are about 30% and should be rectified. In this research the smile effect was corrected by ACORN using prior the launch parameters measured by TRW (a company contracted by NASA to build Hyperion).

A variety of packages for atmospheric correction have been developed, including ATREM, FLAASH, ATCOR, ACORN, and the atmospheric correction module in the GEOMATICA platform. All of these use the MODTRAN radiative transfer algorithm, however, and some of them, like FLAASH and ACORN; have options to share the empirical experience of the user.

According to some previous studies about different algorithms for atmospheric correction, ACORN has proven its reliability. Its only drawback is that applying this method requires a great deal of knowledge about hyperspectral remote sensing (CHANG & DU 2004). ACORN offers different algorithms for atmospheric correction of various sensors (modes 1 to 7) and mod 1 is planned for hyperspectral data. We therefore used ACORN mode 1 for the atmospheric correction of the dataset.

ACORN offers a range of strategies for atmospheric correction. These include both empirical and radiative transfer code based methods for atmospheric correction of both hyperspectral and multispectral datasets.

ACORN also offers several artefact suppression options, as well as single spectrum enhancement options to improve atmospheric correction results. Radiative transfer atmospheric correction of calibrated data uses both the calibrated data and additional specified parameters to derive and model the absorption and scattering characteristics of the atmosphere. These modelled atmospheric characteristics are then used to invert the radiance to apparent surface reflectance.

Available artefacts on ACORN are divided into three types. Type 1 corrects for any mismatch in the spectral calibration of the hyperspectral data and the spectral radiative transfer calculations. It suppresses the artefacts located near the strong atmospheric absorption features at 760, 940, 1150, and 2000 nm. Type 2 identifies and suppresses other small artefacts located across the spectral range due to errors in the absolute radiometric calibration and/or errors in the radiative transfer calculations. The spectrum across the 1,400 and 1,900 nm water vapour bands often produces noisy reflectance results because of the low radiance values recorded in these regions. Type 3 assesses the signal levels of the calibrated radiance and suppresses the lowest signal portions where erroneous reflectance calculations may occur. The result is that the lowest signal portions of the spectrum are set to zero on the apparent surface reflectance output. These artefacts do not manipulate absorption features on the spectral profiles. Fig. 2 il-

lustrates the spectral profiles of a pixel before and after atmospheric correction. All three artefact suppressions were applied.

After applying atmospheric correction and artefact suppressions available in ACORN, some additional tasks like bad band determination and polishing are done to improve the spectral profile quality. This process smoothen noisy fluctuations on spectral profile and small absorption features are probably eliminated.

Briefly, bad bands refer to some bands in the dataset that contain very little or no extractable information. The quality of digital remote sensing data is directly related to the level of the signal to system noise ratio (SNR). Theoretically, the SNR ratio for Hyperion is 190 to 40 as the wavelength increases (PEARLMAN et al. 2000). One common approach to determining an approximate SNR for remote sensing data is to use a mean/standard deviation method. This approach requires defining a spectrally homogeneous area (an area with minimum intrinsic variance), calculating the average spectrum for that area, and determining the spectrally distributed standard deviation for the average spectrum. MANOLAKIS et al. (2003) conducted a survey by analysing approximately 14 Hyperion scenes from around the world using the mean/standard deviation SNR method and showed that there is a strong relationship between the acquisition time of the year (because of the effect of illumination to observation geometries) and the SNR of the Hyperion data. The calculated SNRs for Hy-

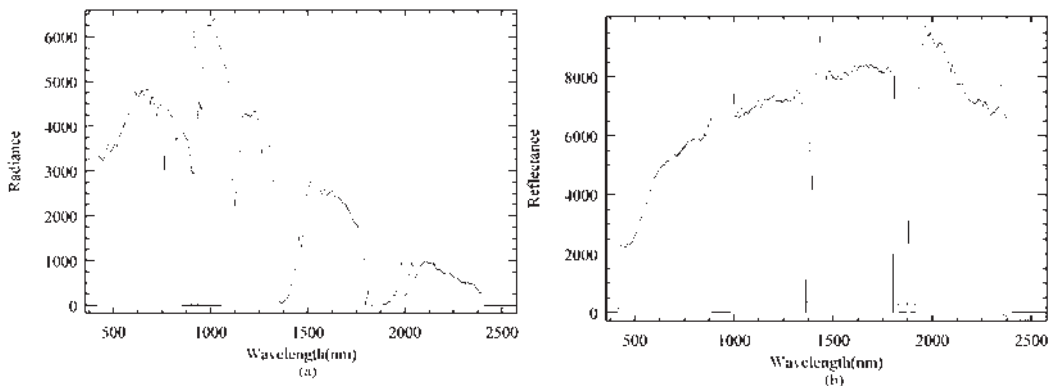


**Fig. 2:** Spectral profile of a pixel before (a) and after (b) atmospheric correction by ACORN; bad bands are marked by dotted ellipses.

perion SWIR data are higher in the summer and lowest in the winter. This has a direct effect on spectral mineral mapping, with lower SWIR SNRs resulting in the extraction of less detail (MANOLAKIS et al. 2003). Fig. 3 illustrates the signal to noise ratio calculated for our Hyperion data by the aforementioned method. According to this plot, uncalibrated channels (channels 1–8 and 222–242) in addition to those affected strongly by water vapour absorption (940 nm, 1,400 nm, 1,900 nm) have zero SNR. These channels are listed in the list of bad bands for the following processing tasks. In addition, the bands that possess lower SNR ratios compared to the nearby channels are also considered to be bad bands.

The effect of an additive noise process,  $n_a$ , on an image digital number (DN) at the  $i^{\text{th}}$  and  $j^{\text{th}}$  pixel can then be modelled as the summation of the true signal,  $S$ , with the noise, as shown by TU et al. (1998):

$$DN(i, j) = S(i, j) + n_a(i, j) \quad (2)$$

If the noise proportion in the above equation is significant, the DNs almost equal the noise amount and the band will be labelled as bad. We used up only good bands (subset 166 good bands of total 242 bands) to avoid any possible mistakes during pre-processing and subsequent steps. As a final pre-processing task, the data were polished using a geostatistical algorithm presented by the author (OSKOU EI & BUSCH 2008).

## 2 Independent Components Analysis

Determining the virtual dimensionality (VD) of a dataset is essential to perform a successful ICA. This is also known as the number of detectable endmembers. The VD was computed using the HARSANYI, FARRAND, and CHANG (HFC) method presented by HARSANYI et al. (1993), and then the Fast fixed-point algorithm for Independent Component Analysis (FastICA) programme was applied to calculate independent components (ICs). Since this program does not prioritise the output ICs, a prioritisation step is also necessary after achieving the ICs. Finally, the abundances of the ICs were calculated for mapping purposes.

### 2.1 Virtual Dimensionality of the Data

The HFC method is presented by HARSANYI et al. (1993) and uses Neyman-Pearson detection theory to estimate the number of endmembers. This idea is described in CHANG & DU (2004) and NASH & JOHNSON (2002).

According to CHANG & DU (2004), the eigenvalues generated by the sample correlation matrix and the sample covariance matrix are denoted by correlation eigenvalues and covariance eigenvalues, respectively. Since the component dimensionality is equal to the total number of eigenvalues, each eigenvalue specifies a component dimension and provides an

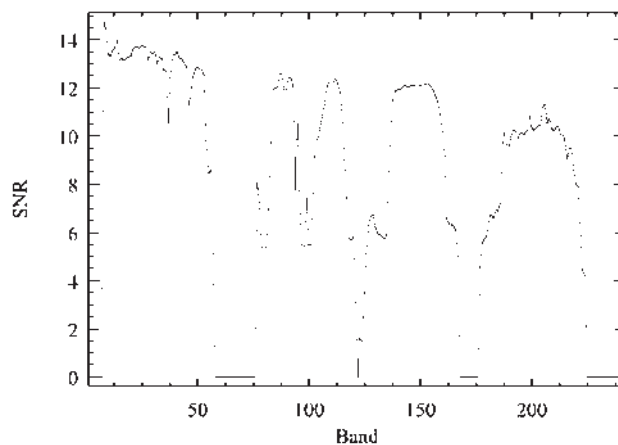


Fig. 3: Signal to noise ratio calculated for Hyperion data by the mean/deviation method.

indication of the significance of that particular component in terms of variance. If there is no signal source contained in a particular component, the corresponding correlation eigenvalue and covariance eigenvalue in this component should reflect only the noise energy, in which case the correlation eigenvalue and covariance eigenvalue are equal. This provides us with a basis from which we can formulate the difference between the correlation eigenvalue and its corresponding covariance eigenvalue as a binary composite hypothesis testing problem. The null hypothesis represents the case of zero difference, while the alternative hypothesis is the case in which the difference is greater than zero. When the Neyman-Pearson test is applied to each pair of correlation eigenvalues and its corresponding covariance eigenvalue, the number of times the test fails indicates how many signal sources are present in the image. In other words, a failure of the Neyman-Pearson test in a component indicates the truth of the alternative hypothesis, which implies that there is a signal source in this particular component. Using this approach, we can estimate the virtual dimensionality with the receiver operating characteristic analysis to evaluate the effectiveness of the decision.

The virtual dimensionality of the image was calculated using various false alarm probabilities (HARSANYI et al. 1993); these are listed in Tab. 1.

Decreasing the false alarm probability ( $P_{fa}$ ) will increase the threshold amount used to compare the correlation and covariance eigenvalues, but after achieving a certain magnitude, it does not have a significant effect on the threshold. Therefore, as mentioned by the innovators of the method,  $10^{-4}$  seems to be a reasonable value and consequently the virtual dimensionality of the data is 37.

## 2.2 Prioritisation

After determining the number of endmembers by HFC (37 endmembers), the FastICA program (HYVÄRINEN 1999, HYVÄRINEN & OJA 2000) was used to compute the demixing matrix. It was not possible to load the image in MATLAB because of the large size of the Hyperion dataset. According to HYVÄRINEN (1999), we therefore resized them by averaging while producing the two dimensional matrix from the Hyperion cube. The averages can be estimated using a smaller sample, whose size may have a considerable effect on the accuracy of the final estimates. The sample points should be chosen separately at every iteration. If the convergence is not satisfactory, one may then increase the sample size (HYVÄRINEN 1999).

The rows of the matrix are equal to the channel number (166), and each row consists of observations for one band. The method presented by WANG & CHANG (2006b) has been used to perform the priority task. They calculated a high order statistical formula as a score for each independent component obtained by FastICA:

$$ps(IC_i) = \frac{(k_i^3)^2}{12} + \frac{(k_i^4 - 3)^2}{48} \quad (3)$$

where  $k_i^3 = \frac{\sum_{n=1}^{MN} (z_n^i)^3}{MN}$ ,  $k_i^4 = \frac{\sum_{n=1}^{MN} (z_n^i)^4}{MN}$  and  $z_n^i$  is the DN of pixel  $n$  in IC  $i$

Previous work, e. g., (WANG & CHANG 2006a), suggested extracting twice the VD, but we ran the ICA to extract all possible ICs (166 ICs), and the prioritisation algorithm based on formula (3) was used to order ICs. Tab. 2 illustrates the first 37 ICs in priority order.

**Tab. 1:** VDs calculated by the HFC method for different false alarm probabilities (Pfa).

$P_{fa}$	$10^{-1}$	$10^{-2}$	$10^{-3}$	$10^{-4}$	$10^{-5}$
VD	43	38	37	37	37

**Tab. 2:** First 37 prior ICs.

18	2	5	1	4	7	6	11	13	16	3	20	19	8	33	39	32	15	35
24	17	50	10	12	22	29	28	31	21	23	41	53	36	9	26	40	30	

The results imply that running FastICA for only 74 ICs (twice the VD calculated by HFC) was enough. After this the demixing ( $W$ ) and whitening matrices obtained from FastICA were multiplied by original data to obtain IC images according to formula (1) and the above 37 priority channels were picked for later processes. The method for normalising the IC abundances introduced by ZHENG et al. (2006) and WANG & CHANG (2006b) was also applied. According to their formula for each endmember pixel  $e_i$ , let  $IC_i$  be the IC from which  $e_i$  was extracted and  $IC_i(r)$  denote the value of each pixel  $r$  in  $IC_i$ . We normalize the absolute value of  $IC_i(r)$ ,  $|IC_i(r)|$  with respect to  $|e_i|$ , the absolute value of  $e_i$  and define its corresponding abundance fraction  $a_{IC_i}(r)$  by

$$a_{IC_i}(r) = \frac{|IC_i(r)| - \min_r |IC_i(r)|}{|e_i| - \min_r |IC_i(r)|} \quad (4)$$

$e_i$  is the maximum of  $|IC_i(r)|$  over all the image pixels in the  $IC_i$

In each channel of this image, the location of any pixel that has a maximum amount for the appropriate IC was noted. Knowing the locations of these pixels helps us to obtain a preliminary evaluation for the independent components and their similarities. In addition, the image of each IC was surveyed visually to recognise ICs that are related to backgrounds. The result demonstrates that some of the IC images have the same extreme pixel, which means that their maximum amount occurred in the same pixels, like ICs 1,4,5,7,10–11, 14–16,18–21,23–35; ICs 2,22,36; and ICs 6,9. It clearly does not mean that they are completely equal ICs, but we can conclude that they are very similar; on the other hand, we cannot distinguish their differences by this method as our only tool to obtain information about them is their spectral profiles.

### 2.3 Mapping Independent Components

The spectral profiles of those extreme pixels are shown in Fig. 4(a). The spectral angle mapper (SAM) was applied to map the distributions of ICs. In the map produced by this method, only 6 ICs show considerable distributions. Studying each of the IC abundances map separately could help one to obtain valuable information about the mineralogy in the region, but preparing a comprehensive map using by them is not really helpful (Fig. 5(b)).

### 2.4 Stepwise Algorithm

The outcomes of the last procedure imply that some useful endmembers are ignored during the process of prioritisation. This is because of the close similarity between some prioritised ICs that share in extreme pixels and prevent us from detecting other purest pixels. The stepwise algorithm presented here yields an exact solution for this problem. Since the ICs with the same extreme pixels cannot be discriminated, they will be considered as one. To do this practically, the extreme pixels of all possible ICs (166 ICs) should be determined and then the ICs are categorised based on their extreme pixels (ICs with the same extreme pixel in one group). Finally the IC with the best priority score represents its group and distributions of these representative ICs are mapped on the scene. The stepwise process of this method is summarised as follows:

- 1) run FastICA for extracting all possible ICs
- 2) change IC images to abundances map according to formula (4)
- 3) find the maxima for each IC (extreme pixels)
- 4) group the ICs with the same extremes
- 5) prioritisation
- 6) select one IC for each group based on their priority score

- 7) classify the dataset by SAM based on the extremes' spectral profiles
- 8) match the spectral profile to the reference data spectra

The application of this algorithm produced 24 prioritised from 166 primary ICs, as illustrated in Tab. 3. Classification of the scene is done by SAM using the spectral profiles of the extreme pixels as profiles of ICs. The resulting map (cf. Fig. 5(c)) shows a considerable distribution for 8 ICs. To identify the mineralogy of each independent component, the spectral

profiles of extreme pixels were compared to the USGS mineral spectral library, which is resampled for the Hyperion wavelengths. The spectral feature fitting (SFF) method was used to perform that task in the short wave infrared region of the spectra because most differences between the endmember profiles are distinguishable in the range of 1971 to 2365  $\mu\text{m}$  according to Fig. 4(b). Several minerals from the SFF lookup table were selected considering their matching scores as indicative of alteration minerals. Tab. 4 illustrates selected minerals for each endmember.

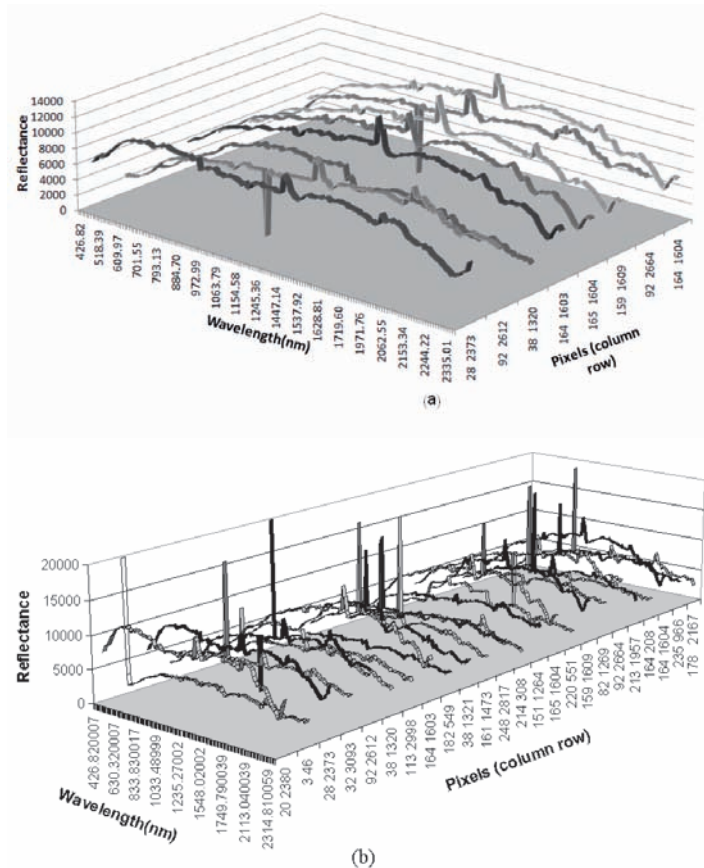


Fig. 4: Spectral profiles of extreme pixels: (a) Ordinary method and (b) Stepwise algorithm.

**Tab. 3:** Extreme pixels of 24 different ICs.

priority	IC	sample	line	priority	IC	sample	line
1	18	20	2380	13	59	214	308
2	2	3	46	14	79	151	1264
3	5	28	2373	15	93	165	1604
4	7	32	3093	16	66	220	551
5	11	92	2612	17	102	159	1609
6	20	38	1320	18	114	82	1269
7	19	113	2998	19	134	92	2664
8	32	164	1603	20	139	213	1957
9	30	182	549	21	152	164	208
10	42	38	1321	22	158	164	1604
11	54	161	1473	23	155	235	966
12	73	248	2817	24	163	178	2167

**Tab. 4:** Minerals that show a high match to 8 mapped ICs.

IC	minerals
5	almandine1, hematitea, almandine3, augite3, diposide3
11	ammonioillite, buddingtonite2, mascagnite, buddingtonite1, alunite2
20	ammoniojarosite, buddingtonite2, mascagnite2, buddingtonite1, hypresthen2
30	axinite, sphalerite4,5, augite3,1, mascagnite1
66	vegetation, mascagnite1,2, galena2, a-jarosite
102	axinite, augite3
134	rivadavite, alunite2, ulexite2, alunite6,4, ulexite1, a-illite, orthoclase, a-smectite
155	a-jarosite, mascagnite2, buddingtonite2, mascagnite1, buddingtonite1, a-chlorite, sphalerite4, acmite, sphalerite5, howlite, pectolite1

### 3 Conclusions

Independent component analysis on the Hyperion data of Erongo led us to present a modified algorithm in this study, as a previous method (WANG & CHANG 2006) was able to detect all possible ICs. Since some ICs share in extreme pixels, only eight ICs were detected by their method. The Hyperion scene is then classified by a spectral angle mapper using the spectral profiles of eight extreme pixels as endmembers. This classifier revealed that only six of them show considerable distribution on the study scene.

The presented method differs from theirs, as in this method extreme pixels for all 166 ICs are determined and all ICs with the same extreme pixels are considered equal. Prioritisation of the IC bands takes place afterward. Therefore, by this method 24 different extreme pixels were recognised, and like the first method, a spectral angle mapper was used for classification. The maps produced by these two methods demonstrate that the second algorithm performs better, because in addition to its ability to map more endmembers, the mapped zones match lithological structures better (Fig. 5 (a) and (b)).

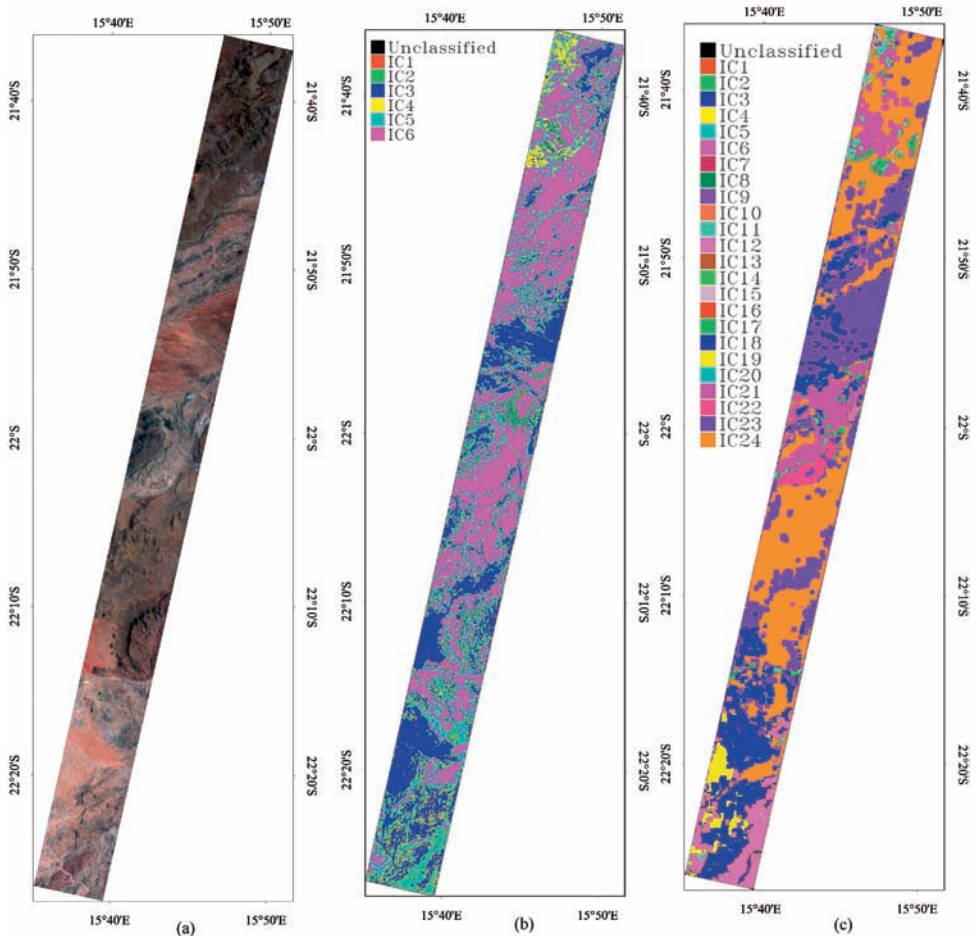


**Fig. 5:** RGB image of Hyperion data (a), ICs distribution map by the Chang method (b) and by the method presented here (c).

## References

- BAYLISS, J.D., GUALTIERI, J.A. & CROMP, R.F., 1998: Analysing hyperspectral data with independent component analysis. – SPIE International Conference, Washington, DC, 133–143.
- BOTCHKO, V., BERINA, E., KOROTKAYA, Z., PARKKINEN, J. & JAASKELAINEN, T., 2003: Independent component analysis in spectral images. – 4th International Symposium on Independent Component Analysis and Blind Signal Separation, Nara, Japan, 203–207.
- CHANG, C.I. & DU, Q., 2004: Estimation of number of spectrally distinct signal sources in hyperspectral imagery. – *IEEE Transactions on Geoscience and Remote Sensing* **42** (3): 608–619.
- CHIANG, S.S., CHANG, C.I. & GINSBERG, I.W., 2000: Unsupervised hyperspectral image analysis using independent component analysis. – *IEEE International Geoscience and Remote Sensing Symposium*, 3136–3138.
- DU, Q., KOPRIVA, I. & SZU, H., 2006: Independent component analysis for hyperspectral remote sensing imagery classification. – *Optical Engineering* **45** (1): 17008.
- HARSANYI, J.C., FARRAND, W. & CHANG, C.I., 1993: Determining the number and identity of spectral endmembers: An integrated approach using Neyman-Pearson eigenthresholding and iterative constrained RMS error minimiza-

- tion. – 9th Thematic Conference on Geologic Remote Sensing, Pasadena, California, USA.
- HYVÄRINEN, A., 1999: Fast and Robust Fixed-Point Algorithms for Independent Component Analysis. – *IEEE Transactions on Neural Networks* **10** (3): 626–634.
- HYVÄRINEN, A. & OJA, E., 2000: Independent Component Analysis: Algorithms and Applications. – *IEEE Transactions on Neural Networks* **13** (4–5): 411–430.
- LENNON, M., MOUCHOT, M., MERCIER, G. & HUBERT-MOY, L., 2001: Spectral unmixing of hyperspectral images with the independent component analysis and wavelet packets. – *IEEE International Geoscience and Remote Sensing Symposium*.
- MANOLAKIS, D., MARDEN, D. & SHAW, G.A., 2003: Hyperspectral Image Processing for Automatic Target Detection Applications. – *Lincoln Laboratory Journal* **14** (1): 79–166.
- NASH, G.D. & JOHNSON, J.W., 2002: Soil mineralogy anomaly detection in Dixie Valley, Nevada using hyperspectral data. – Twenty-Seventh Workshop on Geothermal Reservoir Engineering, Stanford University.
- OSKOEI, M.M. & BUSCH, W., 2008: A geostatistically based preprocessing algorithm for hyperspectral data analysis. – *GIScience & Remote Sensing* **45** (3): 356–368.
- PEARLMAN, J., SEGAL, C., LIAO, L., CARMAN, S., FOLKMAN, M., BROWNE, B., ONG, L. & UNGAR, S., 2000: Development and operations of the eo-1 hyperion imaging spectrometer. – *SPIE Conference on Earth Observing Systems* **4135**: 243–254.
- SCHNEIDER, G.I.C. & SCHNEIDER, M.B., 2004: Gondwanaland Geopark. (Windhoek Cluster Office), Namibia.
- TU, T.M., CHEN, C.H., WU, J.L. & CHANG, C.I., 1998: A fast two-stage classification method for high dimensional remote sensing data. – *IEEE Transactions on Geoscience and Remote Sensing* **36**: 182–191.
- VARSHNEY, P.K. & ARORA, M.K., 2004: Advanced image processing techniques for remotely sensed hyperspectral data. – Springer, Berlin.
- WANG, J. & CHANG, C.I., 2006: Applications of independent component analysis (ICA) in endmember extraction and abundance quantification for hyperspectral imagery. – *IEEE Transactions on Geoscience and Remote Sensing* **44** (9): 2601–2616.
- WANG, J. & CHANG, C.I., 2006: Independent Component Analysis-Based Dimensionality Reduction with Applications in Hyperspectral Image Analysis. – *IEEE Transactions on Geoscience and Remote Sensing* **44** (6): 1586–1600.
- ZHENG, C.H., HUANG, D.S., SUN, Z.L., LYU, M.R. & LOK, T.M., 2006: Nonnegative independent component analysis based on minimizing mutual information technique. – *Neuro Computing* **69**: 878–883.

Address of the Author:

Dr. MAJID MOHAMMADY OSKOEI, Faculty of Mining Engineering, Sahand University of Technology, Tabriz, Iran; Tel: +98(0)4123459-299, Fax: -299, e-mail: moskouei@yahoo.com

Manuskript eingereicht: Juni 2009

Angenommen: Dezember 2009